High Accuracy Real-time Multi-Gas Identification by Batch-Uniform Gas Sensor Array and Deep Learning Algorithm

Mingu Kang, Incheol Cho, Jaeho Park, Jaeseok Jeong, Kichul Lee, Byeongju Lee, Dionisio Del Orbe Henriquez, Kukjin Yoon*, and Inkyu Park*

*Corresponding authors. Emails: kjyoon@kaist.ac.kr (K. Yoon), inkyu@kaist.ac.kr (I. Park)

Department of Mechanical Engineering, Korea Advanced Institute of Science and Technology (KAIST), 291 Daehak-ro, Yuseong-gu, Daejeon, 34141, Republic of Korea

KEYWORDS. Gas sensor array, Electronic nose, Glancing angle deposition, Deep learning, Real-time gas identification.

ABSTRACT: Semiconductor metal oxide (SMO) gas sensors are attracting great attention as the next-generation environmental monitoring sensors. However, there are limitations in the actual applications of SMO gas sensors due to their low selectivity. Although the electronic nose (E-nose) systems based on a sensor array are regarded as a solution for the selectivity issue, poor accuracy caused by the non-uniformity of the fabricated gas sensors and difficulty of real-time gas detection have yet to be resolved. In this study, these problems have been solved by fabricating uniform gas sensor arrays and applying the deep learning algorithm to the data from the sensor arrays. Nanocolumnar films of metal oxides (SnO_2, In_2O_3, WO_3, and CuO) with a high batch uniformity deposited through glancing angle deposition (GLAD) were used as the sensing materials. The convolutional neural network (CNN) using the input data as a matrix form was adopted as a learning algorithm, which could conduct pattern recognition of the sensor responses. Finally, a real-time selective gas detection for CO, NH_3, NO_2, CH_4, and Acetone (C_3H_6O) gas was achieved (minimum response time of 1, 8, 5, 19, and 2 sec, respectively) with an accuracy of 98% by applying preprocessed response data to the CNN.

Recently, the demand for gas monitoring systems keeps increasing due to various damages and air pollutions caused by the leaks of chemical gases from industrial sites and automobile exhausts. Although a gas chromatography, which is one of the most conventional methods to analyze gases, has high accuracy, it has limitations in its portable usage because the equipment is very large and expensive. To overcome the shortcomings of the gas chromatography, various researches on miniaturized gas sensors such as catalytic combustion type,[1,2] electrochemical type,[3,4] optical type,[5] and chemiresistive type[6–9] gas sensors have been actively conducted. Among them, chemiresistive gas sensors are attracting attention as the next-generation gas sensors because they are the most suitable for mobile gas sensors owing to their ultra-small size and low price.[10] There are various types of sensing materials in chemiresistive gas sensors,[8,9,11,12] and semiconductor metal oxide (SMO) is one of the most widely used materials.

The SMO gas sensors use metal oxides as the sensing materials and can detect target gases based on the changes in the resistance of the sensing materials due to the modulation of the electron depletion layer thickness caused by absorption and desorption of the target gases from the surface of the metal oxides.[13] However, because of the simple sensing principle of the SMO gas sensors, they have a critical disadvantage of low selectivity since they can react with all gases that cause the change of the electron depletion layer.[14,15] Therefore, various studies have been conducted to solve the low selectivity problem of the SMO gas sensors, and typical methods are to use catalysts that can provide high sensor responses to specific gases, and filters to penetrate target gases preferentially.[16–20] Nevertheless, the use of catalysts is not able to secure sufficient selectivity when the concentrations of other gases are higher than that of a particular target gas, and also using filters degrades sensing performances of the sensor such as sensitivity and response time.

In order to overcome these limitations, the electronic nose (E-nose) system is in the spotlight as a promising method to increase the selectivity of the SMO gas sensors.[21] The E-nose system, which mimics the human olfactory system, is a method to classify gas types and to predict their concentrations by analyzing the patterns of the sensor responses collected from the sensor array through machine learning.[22,23] The E-nose system can collect response patterns of the gas sensors in different conditions because the sensor array uses multiple types of sensing materials or gas sensors with different driving temperature conditions.[24-27] Since the E-nose system does not directly affect the sensing materials of gas sensors, there are no problems that have been caused by the use of filters or catalysts. In the E-nose system, it is an important issue to ensure the sensor-to-sensor uniformity because the machine learning algorithm, which classifies the target gases and predicts the concentrations, is trained based on the sensors' responses obtained from the sensor array. However, recently developed

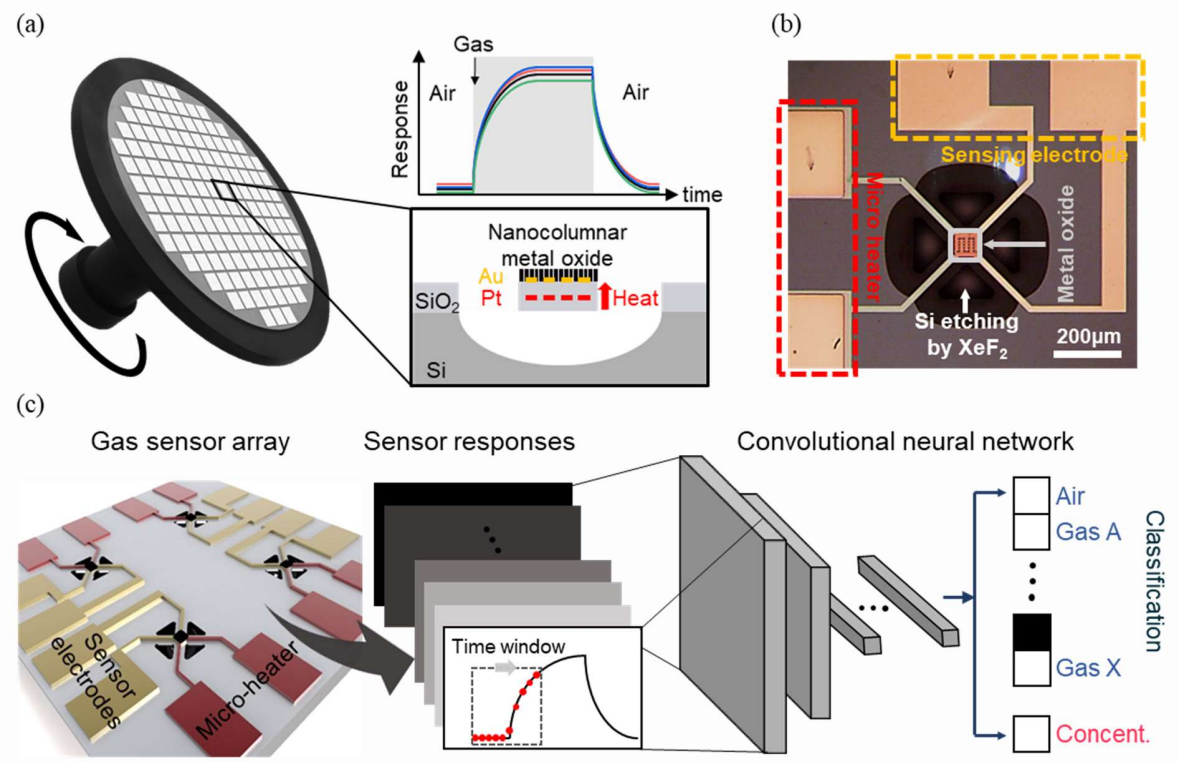

Figure 1. (a) Schematic diagram for the fabrication of high batch-uniform semiconductor metal oxide (SMO) gas sensors using glancing angle deposition (GLAD). (b) Microscopic image of the suspended microheater platform-based SMO gas sensors whose sensing material is with nanocolumnar In_2O_3 thin film deposited through GLAD. (c) Real-time classification and regression of target gases by convolutional neural network (CNN) based analysis of gas sensing data. The CNN consists of a single convolution layer and multiple fully connected layers, for real-time selective gas detection. The input data of the network are the sensor response features that contain the information from the transient region by using the time window, and the output data of the network are both gas types and concentration values of the target gases.

SMO gas sensors have been fabricated by screen printing, electrohydrodynamic printing (EHD), and inkjet printing of sensing materials, which suffer from poor uniformity between fabricated gas sensors due to the low precision of these printing methods.[8,9,28] In addition, traditional machine learning algorithms such as principal components analysis (PCA), support vector machine (SVM), etc. failed to conduct selective gas detection in real-time, because they could only utilize the steady-state responses of the sensor array due to the limitations in their decoding performances.[23-26]

In this study, to ensure the general availability of E-nose systems, a gas sensor array with a uniform sensing performance was fabricated through glancing angle deposition (GLAD) conducted on a wafer-scale (**Figure 1**a).[29–31] SnO_2, In_2O_3, WO_3, and CuO were used as the sensing materials for the SMO gas sensors, and as shown in **Figure 1**b, a micro-electro-mechanical-system (MEMS)-based suspended microheater platform was applied to the SMO gas sensors to meet the high operating temperature conditions required for SMO gas sensors with low power consumption.[8] In addition, by fabricating the sensor control module for heater control and sensor data acquisition, sensing data from the gas sensor array was simultaneously collected in CO, NH_3, NO_2, CH_4, and Acetone (C_3H_6O) gas tests,[32] and it was possible to verify the uniform performance of the SMO gas sensors. Also, by adopting the convolutional neural network (CNN) using the input data as a matrix form without vectorization for selective gas detection,[33] both the information generated from a gas sensor array consisting of various gas sensors and the temporal information, which is the information on time-varying sensing patterns, could be used as the input data. Finally, by applying the CNN to the pre-processed sensor response data with a moving time window, it was possible to utilize the data in the transient region, and real-time selective gas detection was conducted for the SMO gas sensors that were not used for the training algorithm of the CNN (**Figure 1**c).

RESULTS AND DISCUSSION

The GLAD is a fabrication process that performs the physical vapor deposition (PVD) of target materials on a wafer-scale with very high uniformity.[30,34] Also, because the deposition proceeds while the substrate is rotated at a certain angle with respect to the target materials, a nanoscale shadow area is generated by the nanoparticles that first reach the substrate, and thus nanocolumnar thin films are fabricated.[30,31,35,36] In this study, nanocolumnar thin films of 4 types of metal oxides (SnO_2, In_2O_3, WO_3, and CuO) were deposited via RF sputtering at a glancing angle of 85°. SEM images of 4 types of metal oxide thin films are as shown in **Figure 2**a-d, and all types of the metal oxides were

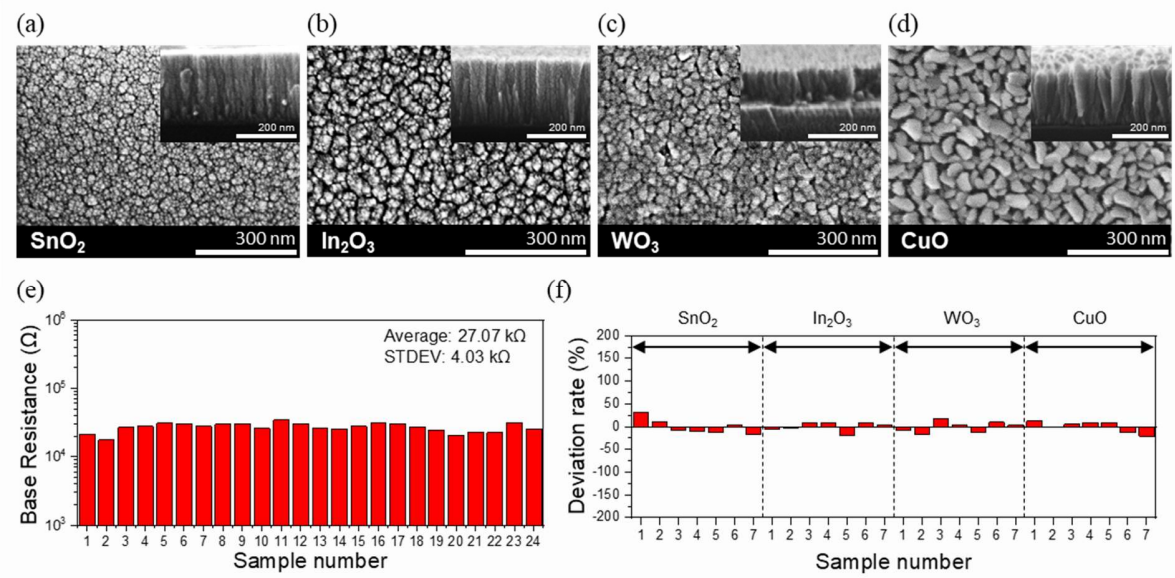

Figure 2. SEM images with top and cross-sectional (inset) views of nanocolumnar metal oxide thin films deposited by a glancing angle deposition (GLAD) method - (a) SnO_2, (b) In_2O_3, (c) WO_3, and (d) CuO. (e) Base resistance distribution of In_2O_3 deposited through GLAD (measurement at the temperature of 250℃ and bias of 3V). The evaluation was performed with 24 samples. (f) Deviation rate of the base resistance of nanocolumnar SnO_2, In_2O_3, WO_3, and CuO thin films on the suspended microheater platform when an electrical power of 11 mW was applied to the microheater to generate the high-temperature condition. The average deviation rate was 15.7%, 10.0%, 11.6%, and 12.4%, respectively.

deposited in the form of nanocolumns, which provides large surface-to-volume ratios of the sensing materials. In **Figure S1**, it is observed that the nanocolumnar thin film deposited through the GLAD has much better sensing performance than the dense thin film deposited through conventional RF sputtering in NO_2 gas test.

In addition, porosity values of the nanocolumnar thin films deposited through the GLAD at 85^0 glancing angle were calculated. Assuming that the film has a prismatic columnar structure, the porosity value was estimated as top-view area of voids / total top-view area × 100 (%). The flow of image processing is shown in **Figure S2**a, and it was possible to automatically capture voids from the top-view SEM image of In_2O_3 films. The voids area was captured through contrast differences in the SEM image using the ImageJ software (auto setting). The area fraction of voids on the In_2O_3 films was calculated by the captured voids area. **Figure S2**b shows the porosity distribution of five different In_2O_3 film samples, and the porosity of the films is very uniform regardless of location in the films (average porosity: 46.42% and standard deviation: 0.61%). Also, the base resistance values of the 24 nanocolumnar In_2O_3 film samples deposited on the sensing electrode array on a 4-inch silicon wafer were measured at 250℃ using a semiconductor analysis equipment. As shown in **Figure 2**e, the average base resistance value of 24 samples was 27.07 kΩ and the standard deviation was 4.03 kΩ, which shows that the distribution of base resistance is reasonably narrow owing to the uniformity of the nanocolumnar films deposited through GLAD. Furthermore, **Figure S2**c shows the dynamic responses (R_{gas}/R_{air}) of the 4 different nanocolumnar In_2O_3 thin films deposited on the sensing electrodes to NH_3 gas, and the relative standard deviation values ($\sigma_{std.}/\mu_{mean} \times 100$ (%)) of the responses for each concentration were very low (about 3.1%). Therefore, through these results, it is confirmed that the nanocolumnar metal oxide thin films deposited through the GLAD have highly uniform resistance values, geometry, and sensing performance.

On the other hand, the uniformity of metal oxide nanofibers printed through the EHD printing was much lower than that of nanocolumnar films deposited through the GLAD. **Figure S3** shows the deviation rate of the base resistance of metal oxide nanofibers patterned on the sensing electrode array using the EHD printing (average base resistance: 22.15 kΩ and standard deviation: 7.86 kΩ for 16 samples), and it is confirmed that the base resistance uniformity of the metal oxide is highly improved using GLAD compared to the EHD printing method. **Figure S4** shows the dynamic responses of 3 different SnO_2 and In_2O_3 nanofibers printed on the sensing electrodes through the EHD printing to the NH_3 gas. The relative standard deviation values of the responses of the gas sensors with SnO_2 and In_2O_3 nanofibers were higher than the values of the gas sensors fabricated through the GLAD (EHD-based SnO_2: 6.7%, EHD-based In_2O_3: 3.4%). Furthermore, when the responses of the gas sensors were quantified as $(R_{air} - R_{gas})/R_{air}$, the relative standard deviation values were much higher than the values of the GLAD-based gas sensors (EHD-based SnO_2: 48.2%, EHD-based In_2O_3: 30.4% vs. GLAD-based In_2O_3: 6.6%). In conclusion, in this study, the nanocolumnar thin films of the metal oxides with high uniformity were successfully fabricated using GLAD process and these films could be used as the sensing materials for the SMO gas sensors.

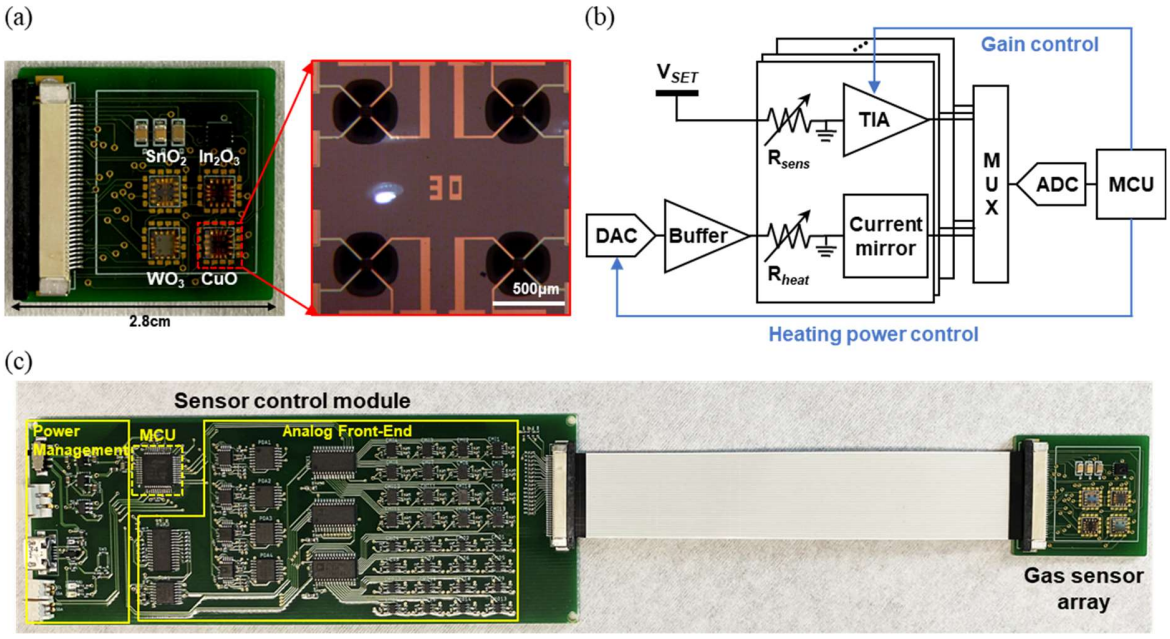

Figure 3. (a) Image of 4×4 suspended microheater platform-based SMO gas sensor array integrated on PCB. (b) Simplified overview of the sensor control module for the gas test. R_{sens} is excited by a DC voltage (2.5 V) from the power management circuit, and the resistance data is converted to the current. The trans-impedance amplifier (TIA) is used to readout a wide sensor resistance range. (c) Image of sensor control module connected to the gas sensor array: Power management part provides stable power to the module, analog front-end drives the microheaters and readouts the sensor signal, and microcontroller unit (MCU) controls the analog front-end components and transmits the sensor responses.

SMO gas sensors are generally operated at high temperatures (200°C to 400°C) to promote the redox reaction of the gases generated on the surface of the metal oxide.[37] In order to provide such a high-temperature environment with low power consumption, SMO gas sensors have used the MEMS-based microheater platform operated by the Joule heating, and the metal oxide is deposited on the microheater to transfer the heat energy to the metal oxide with high efficiency.[38] In this study, a bridge-shaped suspended microheater platform, which has an advantage in low power consumption since the heat leaks only through the thin bridge, was fabricated for the SMO gas sensors according to our previous studies.[8] Afterward, 4 types of metal oxides, SnO_2, In_2O_3, WO_3, and CuO, were deposited on the suspended microheater platform through the GLAD process. The detailed description of the fabrication process of the microheater platform-based gas sensors is provided in the "Experimental Section" and **Figure S5** in the Supporting Information. The fabricated microheater platform generates a temperature condition of 250℃ by applying a power of 11 mW. Evaluation of heating performance of the microheater was conducted without sensing materials, and the heating performance of the microheater is presented in **Figure S6** in the Supporting Information. In addition, as shown in **Figure S7**, we confirmed that the microheater worked very well with a high stability for 12 hours by measuring the resistance change of the microheater while a constant DC power was applied to the heater. In order to evaluate the uniformity of the thin films deposited on the suspended microheater platform, the base resistance values of the metal oxide thin films were measured. **Figure 2**f shows the deviation rate of the base resistance for each metal oxide thin film measured when an electrical power of 11 mW was applied to each microheater. The deviation rate values were quantified as $(R - R_{avg})/R_{avg} \times 100$ (%), and the measurement results demonstrate that the deviation rate for each metal oxide was about 10 %. This result indicates that the metal oxide thin films patterned on the microheater were also highly uniform without chemical changes even after additional fabrication processes such as the XeF_2 etching for the suspended bridge structure formation.[34]

As shown in **Figure 3**a, 4 chips (3.3 mm × 3.3 mm) consisting of 4 gas sensors with each sensing material (SnO_2, In_2O_3, WO_3, and CuO) were integrated into a printed circuit board (PCB), and this gas sensor array was used to check the sensing performance and uniformity of the fabricated gas sensors. In order to collect the sensing responses of the gas sensors in real-time, a module capable of simultaneously driving the gas sensor array is required. Therefore, based on our previous research,[32] an integrated sensor control module for driving the gas sensor array and collecting multiple sensing responses was fabricated. **Figure 3**b shows a simplified overview of the sensor control module, and the module can perform simultaneous feedback control of the electrical power applied to 16 individual microheaters of the sensor array. Furthermore, through a high-precision analog circuit, it can measure a wide range of the resistance values of the sensing materials from 1 kΩ to 1 GΩ. In addition, 16 sensor responses are collected by a microcontroller unit (MCU) through a multiplexer and an analog-to-digital converter, and finally transmitted to the computer. The image of the sensor control module

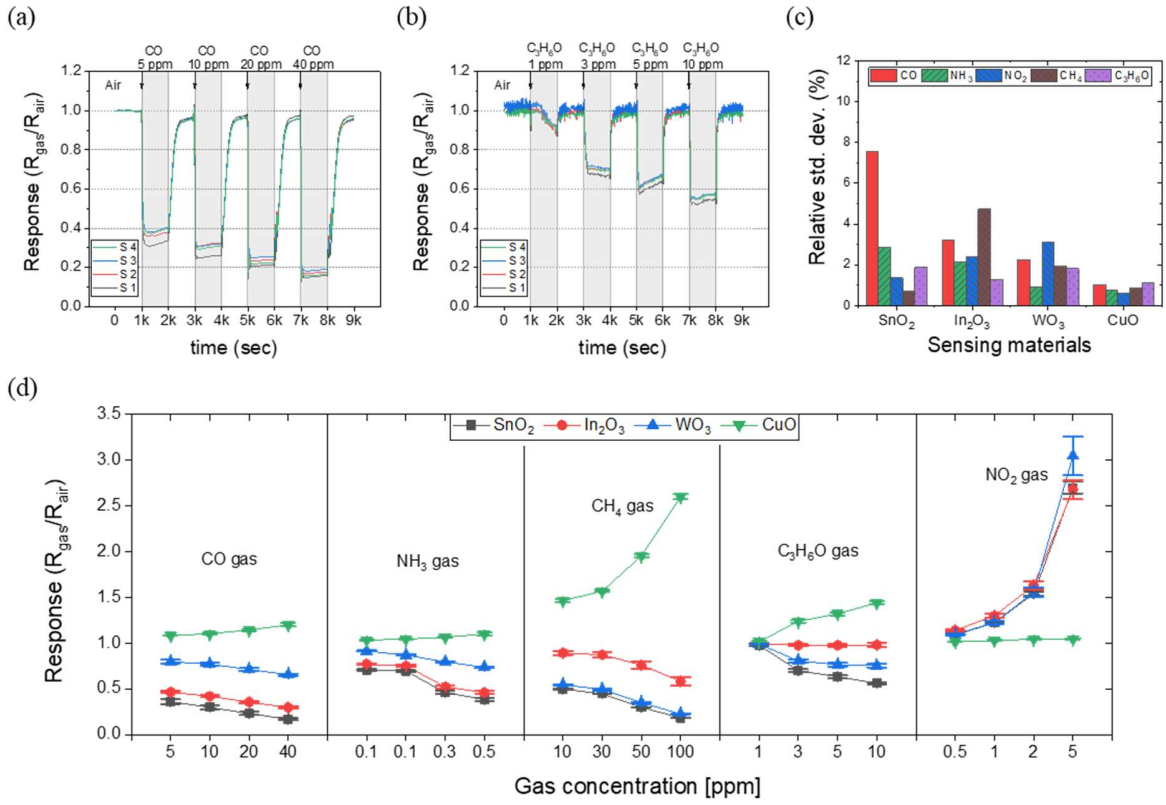

Figure 4. Dynamic responses of the fabricated 4 gas sensors with SnO_2 to (a) CO and (b) C_3H_6O gas when an electrical power of 11 mW was applied to the microheater to generate the high-temperature condition. Shaded and unshaded areas represent the target gas with specified concentrations and synthetic air ambient, respectively. (c) The relative standard deviation of gas sensor response from 4×4 gas sensor array for each sensing material. (d) Responses of the gas sensor array to the target gases and sample-to-sample variation of the responses in each target gas.

connected to the gas sensor array can be seen in **Figure 3**c, and the detailed description of the sensor control module is provided in the "Experimental Section".

In the gas test, CO, NO_2, NH_3, CH_4, and C_3H_6O were used as the target gases, and a gas test setup was constructed using the gas sensor array and sensor control module as shown in **Figure S8** in the Supporting Information. The responses of the gas sensors were quantified as R_{gas}/R_{air}, and 4 gas sensors were used for each sensing material in the gas test. The detailed description of setting conditions for the gas test is provided in the "Experimental Section". **Figure 4**a and b shows the dynamic responses of the 4 gas sensors with SnO_2 to the CO and C_3H_6O gases, and the dynamic responses of the gas sensors were very uniform even with different gas sensors. **Figure S9-S13** shows the dynamic responses of the gas sensor array to the target gases. In order to check the uniformity of the responses of the different gas sensors, relative standard deviation values of the responses were calculated, and the values were around 5 %, which confirms that the fabricated gas sensors have highly uniform sensing performance as well as uniform base resistance (**Figure 4**c). Additionally, as shown in **Figure S14**, repeatability tests were conducted for the CO gas to check the sensing stability of the gas sensor array (S1) when an electrical power of 11 mW was applied to the microheaters. As a result of the tests, there were almost no errors in the sensor responses when repeatedly exposed to the CO gas. Therefore, through the repeatability tests, it is also confirmed that the fabricated gas sensors have an excellent sensing stability at 250℃. **Figure 4**d shows the responses of the gas sensor array to the target gases and sample-to-sample variation of the responses to each target gas. The responses of the n-type semiconductor-based gas sensors (SnO_2, In_2O_3, WO_3) were smaller than 1, and the responses of the p-type semiconductor-based gas sensors (CuO) were larger than 1 to the reducing gases (CO, NH_3, CH_4, and C_3H_6O). On the other hand, in NO_2 gas that is an oxidizing gas, the gas sensor arrays showed the opposite tendency of the responses to the reducing gases. In **Figure 4**d, it can be seen that the responses to the target gases overlap in specific concentration ranges. Therefore, in this study, deep learning algorithm was used to classify the gas types and to predict concentrations by conducting pattern recognition of the sensor responses.

The CNN is a deep learning network that can prevent loss of information that occurs in the process of reducing the dimension of input data because the input data can be used as a matrix without vectorization in the CNN. In this study, by adopting the CNN as a deep learning network for

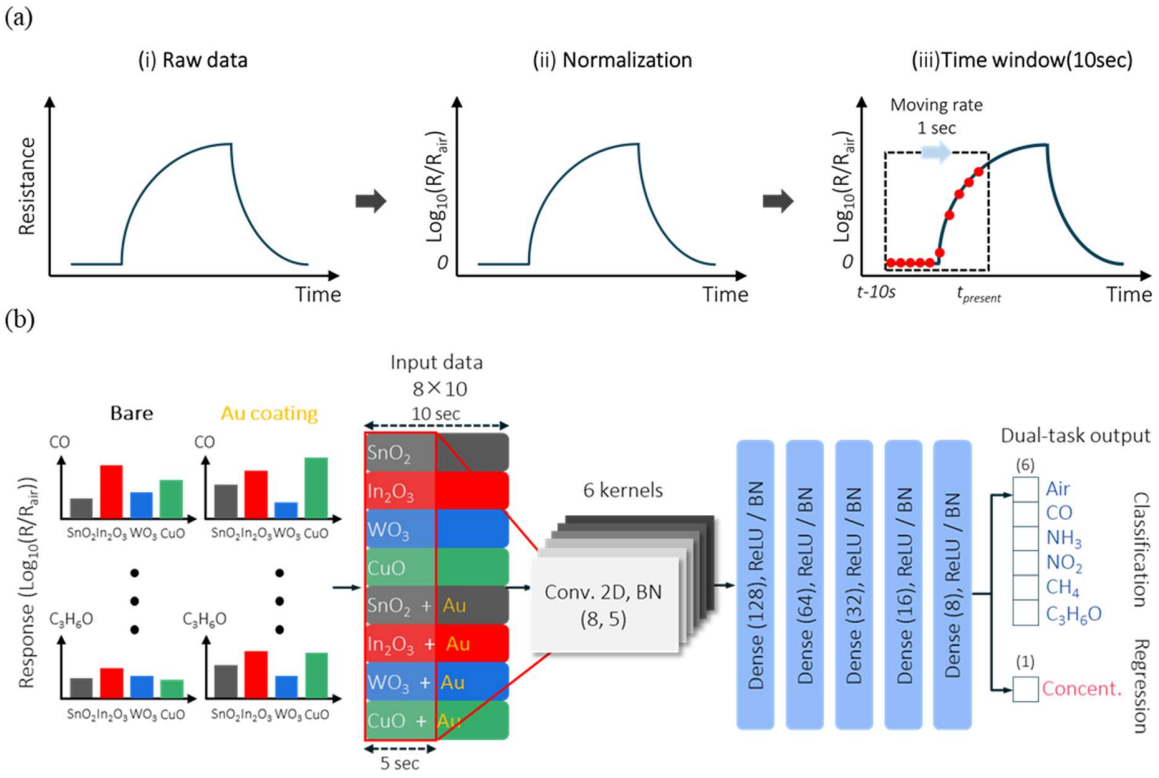

Figure 5. (a) Schematic illustration of pre-processing of the sensing data from the microheater platform-based SMO gas sensor array. (i) shows raw sensing data from the gas sensors. (ii) shows normalized data by using log and base resistance. (iii) shows the method to collect the data with a 10-sec time window. (b) Structure of the convolutional neural network for classifying six gas species (i.e., Air, CO, NH_3, NO_2, CH_4, and C_3H_6O) and for quantifying concentrations of each gas. The network consists of one convolution layer and six fully connected layers (Dense). Six convolutional kernels (8×5) are used to calculate convolution for the feature extraction, and rectified linear unit (ReLU) function is used as an activation function. Batch normalization is conducted in all layers, and the softmax function is used for classification in the output layer

the selective gas detection, both the information generated from a gas sensor array consisting of various gas sensors and the temporal information, which is the information on time-varying sensing patterns, could be used as the input data. Pytorch (Facebook, USA), which is an open-source library for the deep learning, was used to build the CNN with Python language, and the neural network computation was performed in a graphical processing unit (GPU) environment (RTX Titan, NVIDIA, USA). In order to use the gas sensor data collected from the sensor control module as the input data of the CNN and to set the true label of the learning network, data pre-processing was performed as shown in **Figure 5**a. First, normalization was carried out by dividing the resistance of the sensing materials by the base resistance values, and a common log was taken to offset the scale deviation caused by the range of response values depending on the target gas properties. After that, for real-time data pattern analysis, a 10-second time window was applied to input the gas sensing data for 10 seconds into the CNN every second, which made it possible to utilize the information obtained from the transient region. Table S1 shows the labeling of the gas types and concentrations for setting true labels of the deep learning network. The true label for the gas type classification was allocated by using the one-hot-encoding method for a total of 6 cases including air conditions where no target gas exists. In the prediction of the gas concentration, because the gas concentration ranges used in the gas test were different depending on the target gas type, the maximum gas concentration value used in the test for each target gas was normalized to 10, and the normalized concentration was used as the true label for the prediction of the gas concentration.

In this study, gas sensing data collected from the suspended microheater platform-based SMO gas sensor arrays consisting of 4 types of metal oxides with and without Au nanoparticle decoration (1 nm) for five types of target gases were pre-processed by the methods described above, and **Figure S9-S13** and **Figure S15-S19** shows the dynamic responses of the gas sensor arrays to the target gases. The structure of the CNN used to conduct selective gas detection based on the pre-processed data is shown in **Figure 5**b. The pre-processed data was utilized as the input data of CNN in a 8×10 matrix, where 8 is the number for gas sensor types and 10 is the number of sensing data for each gas sensor. In the convolution layer, six kernels were used to perform the convolution operation, and the rectified linear unit (ReLU) was used as an activation function in the operation to minimize the vanishing gradient problem.[39] After the convolution layer, fully connected layers of 128, 64, 32, 16, and 8 nodeswere used with ReLU, and the batch normalization (BN) was carried out to make the distribution of the input data at every layer more uniform.[40] The

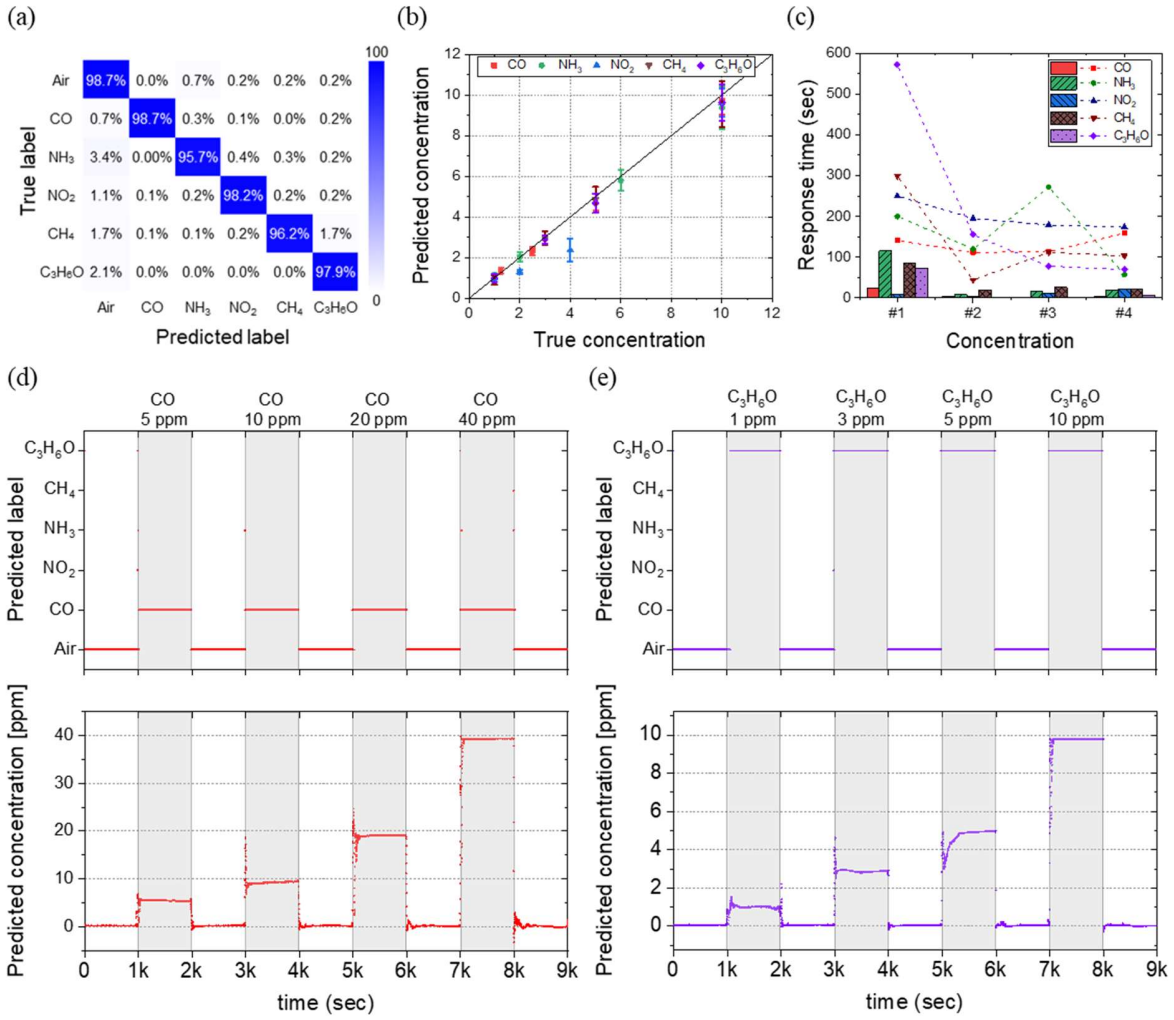

Figure 6. Prediction results of (a) gas types summarized in a confusion matrix and (b) gas concentrations normalized in 0 to 10 for the test data set. (c) Response time that was taken to predict the gas types for the test data set by the proposed E-nose system (bar graph) and the conventional response time spent to reach 90% of the saturated response (scatter graph). Real-time prediction results of gas types and concentrations to the (d) CO and (e) C_3H_6O gases. Shaded and unshaded areas represent the target gas with specified concentrations and synthetic air ambient, respectively

last output layer consisted of 7 nodes using 6 nodes for the gas type classification (Classification) and 1 node for the gas concentration prediction (Regression), and the classification and regression were simultaneously performed. The nodes used for the classification calculated the probability values by using the softmax function as an activation function, and the node used for regression did not use the activation function but predicted normalized concentration values through the regression analysis.

In this study, the categorical cross-entropy and mean squared error were used as the loss function for the classification and regression, respectively, and the CNN was trained by considering both the loss generated in the classification and regression because they were simultaneously performed. Since the loss generated in the classification ($L_{Classification}$) is relatively smaller than that in the regression ($L_{Regression}$) due to the scale differences of the true labels, the total loss for training the CNN was calculated as $L_{total} = 20 \times L_{Classification} + L_{Regression}$. The adoptive moment estimation (Adam) optimizer was used to minimize the total loss of the network,[41] and the CNN was trained for 100 epochs. The data used for the training and validation of the CNN were the shuffled gas sensing data from three different gas sensors in each sensing material for 9,000 seconds in the 5 types of target gas tests ($3 \times 9{,}000 \times 5 = 135{,}000$), and the amount of training data was used twice the amount of validation data. Finally, the test data used for testing the CNN was the sensing data from a new gas sensor array ($1 \times 9{,}000 \times 5 = 45{,}000$) that was not used for training the network, which verifies the general availability of the network.

Based on the CNN described above, the classification and regression were simultaneously performed for the 6 types of gases including air condition every second using the new gas sensing data that was not used for training the network. **Figure 6**a and b shows the result of classifying gas types and prediction of gas concentration. In this study, even using the gas sensor array not used for training the

Table 1. Comparison of gas identification accuracy between the previous studies using electronic nose system and this study.[25,26,42,43]

Ref	Learning algorithm	Number of gas sensors	Number of target gases	Training sensor ≠ Test sensor	Real-time gas identification	Classification accuracy	Quantification average error
Shahid, A. et al.[42]	Artificial neural network	6	2	X	X	98.7%	2.1%
Peng, P. et al.[43]	Convolutional neural network	8	4	X	X	95.2%	-
Tonezzer, M. et al.[25]	Support Vector Machine	5	7	X	X	94.3%	18.4%
Thai, N. et al.[26]	Support Vector Machine	4	5	X	X	100%	14.3%
This study	Convolutional neural network	8	6	O	O	98.1%	10.15%

network, the gas types could be classified very accurately under all situations (total accuracy of classification was 98.06%), and the gas concentration also could be predicted simultaneously with an average error of 10.15%. In addition, the minimum response time to identify the gas types for time for CO, NH_3, NO_2, CH_4, and C_3H_6O was 112, 57, 174, 44, and 70 seconds, respectively) that is a time spent to reach 90% of the saturated response (**Figure 6**c). **Figure 6**d and e shows the real-time prediction results of gas types and concentrations to the CO and C_3H_6O gases, respectively, and the prediction results of the other types of target gases are shown in **Figure S20** in the Supporting Information.

For comparison, the classification for 4 types of gases (Air, CO, NH_3, and NO_2) was performed trough the SVM, a traditional machine learning method. The SVM was conducted using MATLAB (MathWorks, USA) which is an engineering software that provides programming and numerical computing environments. In the SVM, training data set ($6\times9\times3$) and test data set ($3\times9\times3$) were selected from the gas sensor array (S1) in the steady region at each concentration. **Figure S21**a shows the results of the classification using SVM, and the accuracy of the classification was 100%. However, as shown in **Figure S21**b, when sensing data from the transient region for 50 seconds after the target gas (Air, CO, NH_3, and NO_2) injection at each concentration was used as the test data set ($5\times8\times3$), the accuracy of the classification was very poor (60%) since the responses to the target gases overlap in the the transient region. These results show that traditional machine learning algorithms fail to conduct gas identification in real-time even using data from the same gas sensor array used for training the network due to the limitations in decoding performances.

Table **1** shows the accuracy of gas identification in previous E-nose systems and this study. Unlike previous E-nose systems, the proposed method utilizes the gas sensing data of a new gas sensor, which was not used for training the network, as the test data because the performances of the CO, NH_3, NO_2, CH_4, and C_3H_6O was 1, 8, 5, 19, and 2 seconds, respectively, which demonstrates that the gas types could be classified in a much shorter time than the conventional response time (minimum conventional response

fabricated gas sensor arrays were very uniform. Furthermore, the number of test data set is significantly higher compared to the previous E-nose systems because our approach realizes real-time, simultaneous prediction of the gas type and concentration. Despite these conditions, it can be confirmed in Table 1 that the proposed system can identify the target gases with a high degree of accuracy similar to other systems. The real-time prediction of gas type and concentration with a new sensor set that was not used for the training is demonstrated for the first time in the E-nose system to the best knowledge of the authors. As a result, it was possible to overcome the limitations in the previous E-nose systems by fabricating the gas sensors with high batch uniformity to secure the general availability of the E-nose system, and by adopting a deep learning algorithm to conduct selective gas detection in real-time.

CONCLUSION

In this study, we demonstrated an E-nose system that can conduct real-time selective gas detection using batch-uniform gas sensor arrays fabricated through wafer-scale glancing angle deposition and deep learning-based data analysis of multiplexed sensor array. 4 types of metal oxides (SnO_2, In_2O_3, WO_3, and CuO) in the form of a nanocolumnar thin film with high batch uniformity (deviation rate ~ 10%) were used as sensing materials for the gas sensors. A suspended microheater platform was used to generate high-temperature conditions for the sensing materials to detect target gases with low power consumption. CO, NH_3, NO_2, CH_4, and C_3H_6O were used as the target gases, and the gas sensor data were collected using an integrated sensor control module. Through the gas test, it was confirmed that the sensing performances of fabricated gas

sensors were very uniform, with a relative standard deviation of around 5%. Finally, by training the convolutional neural network with the data from the gas sensor array with and without Au nanoparticle decoration, the six types of gas could be classified with about 98% accuracy and their concentrations could be estimated with the 10% error range in real-time. Since the learning algorithms for the pattern recognition of the sensor responses can be used in batch-uniform gas sensors fabricated through GLAD, it is expected to significantly reduce the time and price required to complete the full inspection of sensors and algorithms used in the E-nose systems. Therefore, the proposed system can improve practical uses of the SMO gas sensors in various domestic and industrial IoT applications. In future research, a study related to diversifying the input data parameters (e.g. humidity or temperature) of the system will be continued for robust, accurate, and selective gas detection even in harsh environments such as mixed gas or high humidity situations.

EXPERIMENTAL SECTION

Deposition of sensing materials. 4 types of metal oxide sputtering targets (SnO_2, In_2O_3, WO_3, and CuO) were used for deposition of the sensing materials. They were deposited on gold interdigitated electrodes through GLAD via RF sputtering. Photoresist (AZ5214, MicroChemicals, Germany) that was patterned by UV photolithography was used as a shadow mask, and then lift-off process was carried out to pattern the sensing materials after their deposition. In order to form the nanocolumnar thin films, the deposition was conducted through sputtering at a glancing angle of 85°. The base pressure, working pressure, RF power, Ar gas flow rate, and rotation speed were 1×10^{-6} Torr, 4 mTorr, 250 W, 50 sccm, and 4.0 rpm, respectively. As a result of the deposition process, the average thicknesses of SnO2, In2O3, WO3, and CuO nanocolumnar films were 238 nm, 232 nm, 112 nm, and 210 nm, respectively. For the EHD printing of metal oxide nanofibers, the nanofibers were synthesized by electrospinning process. In order to form printable solutions, the electrospun nanofibers were mixed with ethanol and broken into smaller pieces through the ultrasonication process. After evaporation of the ethanol in a convection oven, the broken pieces of electrospun nanofibers were dispersed in ethylene glycol solvents with 15 wt% concentration. The ethylene glycol ink solution with metal oxide nanofibers was loaded to the syringe that has a needle tip of 90 μm inner diameter. The ink was printed on the sensing electrode by applying a pulse wave bias consisting of base voltage (1.0-1.3 kV) and a jetting voltage (1.2-1.5 kV).

Sensor platform fabrication. For the gas sensing platform, the sensing electrodes were fabricated on a Si substrate. First, the photoresist (AZ5214, MicroChemicals, Germany) was patterned by UV photolithography to pattern the interdigitated gold electrode arrays. Then, an electron beam (E-beam) evaporator was used to deposit a Cr/Au (10 nm/200 nm) layer on the photoresist-patterned wafer followed by lift-off. For the MEMS-based suspended microheater platform, a SiO_2 layer of 1 μm thickness was deposited by plasma-enhanced chemical vapor deposition (PECVD) process on the Si wafer and Ti/Pt (10 nm/200 nm) microheaters were deposited and patterned on the SiO_2 by the E-beam evaporation and the lift-off. Then, for electrical insulation between the sensing electrodes and the microheaters, a SiO_2 layer of 800 nm thickness was deposited by PECVD, and the SiO_2 insulation layer on the heater pads was selectively etched by buffered oxide etchant (BOE) for the electrical contact of the heater pads. After the selective etching of the insulation layer on the heater pads, Cr/Au (10 nm/200 nm thickness) interdigitated sensing electrodes were deposited by the E-beam evaporation. In order to form the Si etching window required for the suspended microheater, photoresist (AZ9260, MicroChemicals, Germany) was coated and patterned, and SiO_2 was etched by reactive ion etching (RIE). Next, after depositing the sensing materials through GLAD via RF sputtering (in case of Au decorated gas sensors, Au nanoparticles were additionally deposited by E-beam evaporation with a deposition thickness of 1 nm), they were patterned by the lift-off. After that, the annealing was performed in a N_2 ambient at 400℃ for 2 hours by a furnace to release the residual stress of the SiO_2 layer and to anneal the sensing layers. Finally, by etching Si of the etching window region through the XeF_2 vapor etching, the suspended microheater platform-based SMO gas sensors were fabricated.

Sensor control module. The sensor control module can be driven by a 5 V USB power source, and the module system contains three parts: power management part, analog front-end (AFE) part, and microcontroller unit (MCU). In the power management part, the charge controller (LM3658, TI, USA) operates in low-dropout mode to generate a constant voltage of 4.2 V. Then, a buck-boost converter converts this voltage to 3.3 V. The AFE can control power applied to the suspended microheaters and drive the metal oxide gas sensors. In this part, a constant voltage is applied to the sensing materials of gas sensors so that a current corresponding to the resistance of the sensing materials flows. Also, for flexible power control of the microheater, a digital-to-analog converter (AD5314, Analog Devices, USA) is used, and a current monitoring chip (ADL5315, Analog Devices, USA) is used to monitor the current through the microheater. Data from the gas sensor array is transmitted to the MCU (ATSAMD21G, Atmel, USA) by using an analog-to-digital converter (AD7091R-8, Analog Devices, USA). Also, for the power control of the microheater and the gain control of the trans-impedance amplifier (AD8574, Analog Devices, USA), a software-based algorithm is conducted.

Characterization of sensing materials and sensors. In order to measure the base resistance of the nanocolumnar metal oxide thin films, a voltage of 3.0 V was applied to the sensing electrodes of the gas sensing platform, and the currents through the sensors were measured by a semiconductor analyzer (4155A, Hewlett-Packard, USA). Gas detection tests for CO, NH_3, NO_2, CH_4, and C_3H_6O gases were conducted using the suspended microheater platform-based SMO gas sensors located in a gas chamber. Mass flow

controllers (AFC500, Atovac, KOREA) can control the concentrations of each gas injected into the gas chamber, and the concentration ranges tested for CO, NO_2, NH_3, CH_4, and C_3H_6O were from 5 ppm to 40 ppm, 0.05 ppm to 0.5 ppm, 0.5 ppm to 5 ppm, 10 ppm to 100 ppm, and 1 ppm to 10 ppm, respectively. Instead of using external heat energy, the gas tests were conducted while the sensing materials with and without Au nanoparticle decoration were heated by using the microheaters that were powered by 11 mW and 15 mW, respectively. The current through the sensing materials was measured by a bias of 2.5 V applied to the sensing electrodes using the sensor control module while the gas sensors were exposed to the gases.

ASSOCIATED CONTENT

Supporting Information.

This material is available free of charge via the Internet at http://pubs.acs.org

Dynamic responses of In_2O_3 deposited by GLAD and conventional sputtering to NO_2 gas, flow of image processing to calculate the area fraction, porosity distribution of nanocolumnar In_2O_3 films, dynamic responses of four different gas sensors based on nanocolumnar In_2O_3 film to NH_3 gas, deviation rate of the base resistance of SnO_2 nanofibers patterned by EHD printing, dynamic responses of gas sensors with SnO_2 and In_2O_3 nanofibers printed through EHD printing to NH_3 gas, detailed fabrication process of the SMO gas sensor, heating performance of the microheater, schematic diagram of the gas test setup, dynamic responses of the SMO gas sensors with and without Au nanoparticle decoration (1 nm) to five types of target gases, real-time prediction results to the NH_3, NO_2, and CH_4 gases, classification results to the Air, CO, NH_3, and NO_2 gases via SVM, and labeling of the gas types and gas concentrations (PDF)

AUTHOR INFORMATION

Corresponding Author

*E-mail: kjyoon@kaist.ac.kr

*E-mail: inkyu@kaist.ac.kr

Author Contributions

The manuscript was written through contributions of all authors. M.K. performed all experiments, analyzed the data, and wrote the paper. M.K., I.C., J.P., K.L., B.L., and D.D.O.H. discussed the fabrication of the gas sensors and sensor control module. M.K., I.C., and J.J. discussed the results of deep learning model. K.Y. and I.P. supervised the project. All authors have given approval to the final version of the manuscript.

Notes

The authors declare no competing financial interest.

ACKNOWLEDGMENT

This work was supported by Multi-Ministry collaborative R&D Program (Development of Techniques for Identification and Analysis of Gas Molecules to Protect Against Toxic Substances) through the National Research Foundation of Korea (NRF) funded by KNPA, MSIT, MOTIE, ME, NFA(NRF-2017M3D9A107386322). This work was also supported by National Research Foundation of Korea (NRF) grant funded by the Korean government (MSIT) (No. 2021R1A2C3008742).

REFERENCES

(1) Liu, F.; Zhang, Y.; Yu, Y.; Xu, J.; Sun, J.; Lu, G. Enhanced Sensing Performance of Catalytic Combustion Methane Sensor by Using Pd Nanorod/γ-Al_2O_3. *Sens. Actuators, B* **2011,** 160 (1), 1091–1097.

(2) Del Orbe Henriquez, D.; Cho, I.; Yang, H.; Choi, J.; Kang, M.; Chang, K. S.; Jeong, C. B.; Han, S. W.; Park, I. Pt Nanostructures Fabricated by Local Hydrothermal Synthesis for Low-Power Catalytic-Combustion Hydrogen Sensors. *ACS Appl. Nano Mater.* **2021,** 4 (1), 7–12.

(3) Zhang, J.; Jiang, G.; Goledzinowski, M.; Comeau, F. J. E.; Li, K.; Cumberland, T.; Lenos, J.; Xu, P.; Li, M.; Yu, A.; Chen, Z. Green Solid Electrolyte with Cofunctionalized Nanocellulose/Graphene Oxide Interpenetrating Network for Electrochemical Gas Sensors. *Small Methods* **2017,** 1 (11), 1700237.

(4) Zhang, J.; Jiang, G.; Cumberland, T.; Xu, P.; Wu, Y.; Delaat, S.; Yu, A.; Chen, Z. A Highly Sensitive Breathable Fuel Cell Gas Sensor with Nanocomposite Solid Electrolyte. *InfoMat* **2019,** 1 (2), 234–241.

(5) Rakow, N. A.; Suslick, K. S. A Colorimetric Sensor Array for Odour Visualization. *Nature* **2000,** 406, 2–5.

(6) Korotcenkov, G. Metal Oxides for Solid-State Gas Sensors: What Determines Our Choice? *Mater. Sci. Eng., B* **2007,** 139 (1), 1–23.

(7) Yang, D.; Kim, D.; Ko, S. H.; Pisano, A. P.; Li, Z.; Park, I. Focused Energy Field Method for the Localized Synthesis and Direct Integration of 1D Nanomaterials on Microelectronic Devices. *Adv. Mater.* **2015,** 27 (7), 1207–1215.

(8) Kang, K.; Yang, D.; Park, J.; Kim, S.; Cho, I.; Yang, H. H.; Cho, M.; Mousavi, S.; Choi, K. H.; Park, I. Micropatterning of Metal Oxide Nanofibers by Electrohydrodynamic (EHD) Printing towards Highly Integrated and Multiplexed Gas Sensor Applications. *Sens. Actuators, B* **2017,** 250, 574–583.

(9) Cho, I.; Sim, Y. C.; Cho, M.; Cho, Y. H.; Park, I. Monolithic Micro Light-Emitting Diode/Metal Oxide Nanowire Gas Sensor with Microwatt-Level Power Consumption. *ACS Sens.* **2020,** 5 (2), 563–570.

(10) Neri, G. First Fifty Years of Chemoresistive Gas Sensors. *Chemosensors* **2015,** 3 (1), 1–20.

(11) Shehada, N.; Cancilla, J. C.; Torrecilla, J. S.; Pariente, E. S.; Brönstrup, G.; Christiansen, S.; Johnson, D. W.; Leja, M.; Davies, M. P. A.; Liran, O.; Peled, N.; Haick, H. Silicon Nanowire Sensors Enable Diagnosis of Patients via Exhaled Breath. *ACS Nano* **2016,** 10 (7), 7047–7057.

(12) Mousavi, S.; Kang, K.; Park, J.; Park, I. A Room Temperature Hydrogen Sulfide Gas Sensor Based on Electrospun Polyaniline-Polyethylene Oxide Nanofibers Directly Written on Flexible Substrates. *RSC Adv.* **2016,** 6 (106), 104131–104138.

(13) Franke, M. E.; Koplin, T. J.; Simon, U. Metal and Metal Oxide Nanoparticles in Chemiresistors: Does the Nanoscale Matter? *Small* **2006,** 2 (1), 36–50.

(14) Dey, A. Semiconductor Metal Oxide Gas Sensors: A Review. *Mater. Sci. Eng., B* **2018,** 229, 206–217.

(15) Bochenkov, V. E.; Sergeev, G. B. Sensitivity, Selectivity, and Stability of Gas-Sensitive Metal-Oxide Nanostructures. *Met. Oxide Nanostruct. Their Appl.* **2010,** 3, 31–52.

(16) Wang, C.; Yin, L.; Zhang, L.; Xiang, D.; Gao, R. Metal Oxide Gas Sensors: Sensitivity and Influencing Factors. *Sensors* **2010,** 10 (3), 2088–2106.

(17) Kim, J. H.; Wu, P.; Kim, H. W.; Kim, S. S. Highly Selective Sensing of CO, C_6H_6, and C_7H_8 Gases by Catalytic Functionalization with Metal Nanoparticles. *ACS Appl. Mater. Interfaces* **2016,** 8 (11), 7173–7183.

(18) Kim, N. H.; Choi, S. J.; Kim, S. J.; Cho, H. J.; Jang, J. S.; Koo, W. T.; Kim, M.; Kim, I. D. Highly Sensitive and Selective

Acetone Sensing Performance of WO_3 Nanofibers Functionalized by Rh_2O_3 Nanoparticles. *Sens. Actuators, B* **2016,** 224, 185–192.

(19) Drobek, M.; Kim, J. H.; Bechelany, M.; Vallicari, C.; Julbe, A.; Kim, S. S. MOF-Based Membrane Encapsulated ZnO Nanowires for Enhanced Gas Sensor Selectivity. *ACS Appl. Mater. Interfaces* **2016,** 8 (13), 8323–8328.

(20) Güntner, A. T.; Abegg, S.; Wegner, K.; Pratsinis, S. E. Zeolite Membranes for Highly Selective Formaldehyde Sensors. *Sens. Actuators, B* **2018,** 257, 916–923.

(21) Park, S. Y.; Kim, Y.; Kim, T.; Eom, T. H.; Kim, S. Y.; Jang, H. W. Chemoresistive Materials for Electronic Nose: Progress, Perspectives, and Challenges. *InfoMat* **2019,** 1 (3), 289–316.

(22) Persaud, K.; Dodd, G. Olfactory System Using a Model Nose. *Nature* **1982,** 299, 352–355.

(23) Kang, H.; Cho, S. Y.; Ryu, J.; Choi, J.; Ahn, H.; Joo, H.; Jung, H. T. Multiarray Nanopattern Electronic Nose (E-Nose) by High-Resolution Top-Down Nanolithography. *Adv. Funct. Mater.* **2020**, 30

(24) Moon, H. G.; Jung, Y.; Han, S. D.; Shim, Y. S.; Shin, B.; Lee, T.; Kim, J. S.; Lee, S.; Jun, S. C.; Park, H. H.; Kim, C.; Kang, C. Y. Chemiresistive Electronic Nose toward Detection of Biomarkers in Exhaled Breath. *ACS Appl. Mater. Interfaces* **2016**, 8 (32), 20969-20976.

(25) Tonezzer, M. Selective Gas Sensor Based on One Single SnO2 Nanowire. *Sens. Actuators, B* **2019**, 288, 53–59.

(26) Thai, N. X.; Tonezzer, M.; Masera, L.; Nguyen, H.; Duy, N. Van; Hoa, N. D. Multi Gas Sensors Using One Nanomaterial, Temperature Gradient, and Machine Learning Algorithms for Discrimination of Gases and Their Concentration. *Anal. Chim. Acta* **2020,** 1124, 85–93.

(27) Acharyya, S.; Jana, B.; Nag, S.; Saha, G.; Guha, P. K. Single Resistive Sensor for Selective Detection of Multiple VOCs Employing SnO2 Hollowspheres and Machine Learning Algorithm: A Proof of Concept. *Sens. Actuators, B* **2020**, 321 (15), 128484.

(28) Ghani, F.; Raza, A.; Kyung, D.; Kim, H. S.; Lim, J. C.; Nah, I. W. Optimization of Synthesis Conditions of High–Tap Density $FeVO_4$ Hollow Microspheres via Spray Pyrolysis for Lithium–Ion Batteries. *Appl. Surf. Sci.* **2019,** 497, 143718.

(29) Wang, J.; Shao, J.; Yi, K.; Fan, Z. Layer Uniformity of Glancing Angle Deposition. *Vacuum* **2005,** 78 (1), 107–111.

(30) Wongchoosuk, C.; Wisitsoraat, A.; Phokharatkul, D.; Horprathum, M.; Tuantranont, A.; Kerdcharoen, T. Carbon Doped Tungsten Oxide Nanorods NO_2 Sensor Prepared by Glancing Angle RF Sputtering. *Sens. Actuators, B* **2013,** 181 (2), 388–394.

(31) Yoon, M.; Lee, S.; Lee, D.; Kim, J.; Moon, J. All-Solid-State Thin Film Battery Based on Well-Aligned Slanted LiCoO 2 Nanowires Fabricated by Glancing Angle Deposition. *Appl. Surf. Sci.* **2017,** 412, 537–544.

(32) Suh, J. H.; Cho, I.; Kang, K.; Kweon, S. J.; Lee, M.; Yoo, H. J.; Park, I. Fully Integrated and Portable Semiconductor-Type Multi-Gas Sensing Module for IoT Applications. *Sens. Actuators, B* **2018,** 265, 660–667.

(33) Lecun, Y.; Bottou, L.; Bengio, Y.; Haffner, P. Gradient-Based Learning Applied to Document Recognition. *Proc. IEEE* **1998,** 86 (11), 2278-2324.

(34) Choi, K. W.; Lee, J. S.; Seo, M. H.; Jo, M. S.; Yoo, J. Y.; Sim, G. S.; Yoon, J. B. Batch-Fabricated CO Gas Sensor in Large-Area (8-inch) with Sub-10 mW Power Operation. *Sens. Actuators, B* **2019,** 289, 153–159.

(35) Moon, H. G.; Choi, Y. R.; Shim, Y. S.; Choi, K. Il; Lee, J. H.; Kim, J. S.; Yoon, S. J.; Park, H. H.; Kang, C. Y.; Jang, H. W. Extremely Sensitive and Selective NO Probe Based on Villi-like WO_3 Nanostructures for Application to Exhaled Breath Analyzers. *ACS Appl. Mater. Interfaces* **2013,** 5 (21), 10591–10596.

(36) Oros, C.; Horprathum, M.; Wisitsoraat, A.; Srichaiyaperk, T.; Samransuksamer, B.; Limwichean, S.; Eiamchai, P.; Phokharatkul, D.; Nuntawong, N.; Chananonnawathorn, C.; Patthanasettakul, V.; Klamchuen, A.; Kaewkhao, J.; Tuantranont, A.; Chindaudom, P. Ultra-Sensitive NO_2 Sensor Based on Vertically Aligned SnO_2 Nanorods Deposited by DC Reactive Magnetron Sputtering with Glancing Angle Deposition Technique. *Sens. Actuators, B* **2016,** 223 (2), 936–945.

(37) Park, C. O.; Akbar, S. A. Ceramics for Chemical Sensing. *J. Mater. Sci.* **2003,** 38 (23), 4611–4637.

(38) Briand, D.; Courbat, J. Micromachined Semiconductor Gas Sensors. In *Semiconductor Gas Sensors*; Jaaniso, R., Tan, O. K. Eds., Woodheaad Publishing Series in Electronics and Optical Materials Number 38; Woodhead Publishing Limited, 2013; ISBN 978-0-85709-236-6, pp 220-260.

(39) Nair, V.; Hinton, G. E. Rectified Linear Units Improve Restricted Boltzmann Machines. *27th Int. Conf. Mach. Learn.* **2010,** 807–814.

(40) Ioffe, S.; Szegedy, C. Batch Normalization: Accelerating Deep Network Training by Reducing Internal Covariate Shift. *32nd Int. Conf. Mach. Learn.* **2015,** 1, 448–456.

(41) Kingma, D. P.; Ba, J. L. Adam: A Method for Stochastic Optimization. *3rd Int. Conf. Learn. Represent* **2015,** 1–15.

(42) Shahid, A.; Choi, J. H.; Rana, A. U. H. S.; Kim, H. S. Least Squares Neural Network-Based Wireless E-Nose System Using an SnO2 Sensor Array. *Sensors* **2018,** 18 (5), 1446.

(43) Peng, P.; Zhao, X.; Pan, X.; Ye, W. Gas Classification Using Deep Convolutional Neural Networks. *Sensors* **2018,** 18 (1), 157.

Table of Contents Graphic